Outer-layer self-similarity of the turbulent boundary layer based on the turbulent/non-turbulent interface

Letian Chen [1], Zhanqi Tang [1,2,*] Ziye Fan [1] and Nan Jiang[1,2]

[1]*Department of Mechanics, Tianjin University, Tianjin 300350, China*
[2]*Tianjin Key Laboratory of Modern Engineering Mechanics, Tianjin 300350, China*

In this paper, we report on the outer-layer self-similarity of the turbulent boundary layer (TBL) from the perspectives of the turbulent/non-turbulent (T/NT) interface. We receive support from the experimental database of the TBL. The database is measured with particle image velocimetry (PIV) at low to moderate Reynolds number range ($Re_\tau = 389$–1000). The T/NT interface is detected by the local turbulent kinetic energy method. The intermittency in the outer layer is considered in the velocity decomposition. From our interface perspective, the exponential self-similarity from the mean streamwise velocity is discovered in the outer region. This indicates the consistency of turbulence characteristics in the turbulent region. The outer-layer self-similarity exists above the logarithmic region and below the region linked to the T/NT interface. Based on the two-point correlation, the consistency of the structural spatial characteristics is revealed. Interface-based turbulent fluctuations suggest that the wall-normal scale of the outer-layer structure not only relates to the height from the wall but also needs to consider the distance to the interface. The energy superposition effect of the outer-layer structure is modeled by the structural spatial characteristics. According to the energy superposition effect, for different interface conditions, the structural-based reconsidered turbulent kinetic energy in the outer region is consistent under the interface-based self-similar frame. The proposed interface-based perspective emphasizes that study in the outer intermittent region should not unilaterally consider the wall reference frame. At the same time, the turbulence characteristics in the intermittent region is self-similar from this interface-based reference framework.

I. INTRODUCTION

The physical mechanism of the turbulent boundary layer (TBL) with multiscale interaction and stratified features is a field that still needs to be worked on. Since the development of experimental techniques [1–4] and computational resources [5–7], the understanding of the TBL has gradually improved.

The TBL is a typical shear flow phenomenon and therefore has stratified characteristics along the wall-normal direction. In the near-wall region, the viscous effect plays an important role [8–10], resulting in the viscous sublayer and the buffer layer ($y^+ < 30$) [11]. The superscript $+$ represents the inner scale ν/u_τ dimensionless method, where ν is the kinematic viscosity, and u_τ is the friction velocity. In the logarithmic region ($30\nu/u_\tau < y < 0.15\delta_{99}$) [11], both viscous and inertial forces are important. Here, δ_{99} is the nominal thickness of the boundary layer, which is defined by 99% of the free-stream velocity u_∞. In the logarithmic region, the hairpin vortex structure is widely distributed [3,12]. The hierarchical hairpin packet conceptual model [3] incorporates the

---

*zhanqitang@tju.edu.cn

viscous-based shear process as well as the inertia-based Townsend's attached eddy hypothesis [13–15]. The fully turbulent region is the key preoccupation of previous turbulence research. In the wake region, the inertial force becomes the dominant term [16]. The undulation of large-scale structures in the wake region leads to the outer-layer intermittency, which connects with the interaction between the turbulent components and non-turbulent components [2,17].

The outer-layer intermittency results from the interaction between the TBL (turbulent components) and the external unrotated flow (non-turbulent components). The concept of the turbulent/non-turbulent (T/NT) interface [1] is introduced to separate the turbulent and non-turbulent components. In the T/NT interface, the conditional mean profiles of the velocity, enstrophy, etc., exhibit a jump [18]. The physical quantity characterizing the intermittency is the intermittency factor (γ) [17,19] which describes the fraction of turbulent components. For the TBL, the distribution of the intermittency factor shows that the outer-layer intermittent region ranges from $0.4\delta_{99}$ to $1.2\delta_{99}$ [17,20]. The intermittency factor in the logarithmic region is $\gamma \rightarrow 1$, and the T/NT interface hardly ever reaches this region [15,21]. This indicates that the outer-layer intermittency has little effect on the full turbulent logarithmic region [22,23]. In the logarithmic region, the streamwise scale of the superstructure [24–26] is much larger than the turbulent bulges [17,27]. The bursting of the turbulent bulges leads to the outer-layer intermittency; that means $\gamma < 1$. The turbulent bulges maintain the Reynolds stresses in the wake region and lead to the growth of the TBL [17]. The turbulent bulges come from the hairpin vortex packets extending to the edge of the boundary layer [3,28]. At the same time, the turbulent fluctuations or turbulent kinetic energy (TKE) are transported toward the edge of the TBL.

Compared with the traditional wall perspective, the interface-based perspective allows the researcher to make an observation. From the interface perspective, the high interface corresponds to the low-speed structure statistically, while the low interface is the opposite and forms the non-turbulent valley [22]. The high- and low-speed large-scale structures are observed as quasiperiodic arrangements in the streamwise direction [29]. This kind of phenomenon stems from the turbulent bulges formed as the byproduct of those hairpin vortex packets intermittently entering the wake region [28,30]. They leave corresponding traces on the spatial modes of the proper orthogonal decomposition as well as on the two-point correlation function [15,29]. The geometric features of the T/NT interface, such as interface height and inclination angle, are correlated with the outer-layer structures in the wake region. Lee *et al.* [27] suggested that the large-scale structure has a modulating effect on the T/NT interface shape. The high-speed structure leads to the wedge deformation of the T/NT interface. This effect causes the angles of the interface to show anticorrelation with the internal shear layer. The low-speed structure correlates with the wave peak of the T/NT interface. The characteristic length of the T/NT interface fluctuations is comparable with the boundary layer thickness [21] and the characteristic scale of large-scale turbulent bulges [17]. This suggests the obvious correlation between the outer-layer structures and the characterization of the local interface. However, interface-based conditional statistics are performed only in rough interval divisions. The outer-layer structure characteristics based on the interface perspective are only stated in the framework of the dichotomy between high and low interface. More systematic elaboration is still lacking.

The scaling and dynamics of the T/NT interface are revealed under the T/NT interface frame [31–35]. The interface has fractal characteristics, and the fractal dimension is $\sim$2.3–2.4 [32], which indicates that the T/NT interface shows the multiscale characteristic. The continuous interfacial layer is composed of the viscous superlayer [1] and the turbulent sublayer [34,36]. For the TBL, the thickness of the T/NT interface is 0.5–0.7 times the Taylor microscale [33,34]. The coherent vortices near the T/NT interface are preferentially aligned with the tangent to the T/NT interface [31]. The radii of these coherent vortices are on the order of the Taylor microscale [31]. The dynamics in the vicinity of the interface, such as the entrainment motion [21], has relatively independent mechanisms respecting the entire outer region. This suggests that coherent structures close to the interface have a relatively small scale. Associated with the conclusions from the wall perspective, the scale of the outer-layer structure increases with height from the wall [37], reaches a maximum,
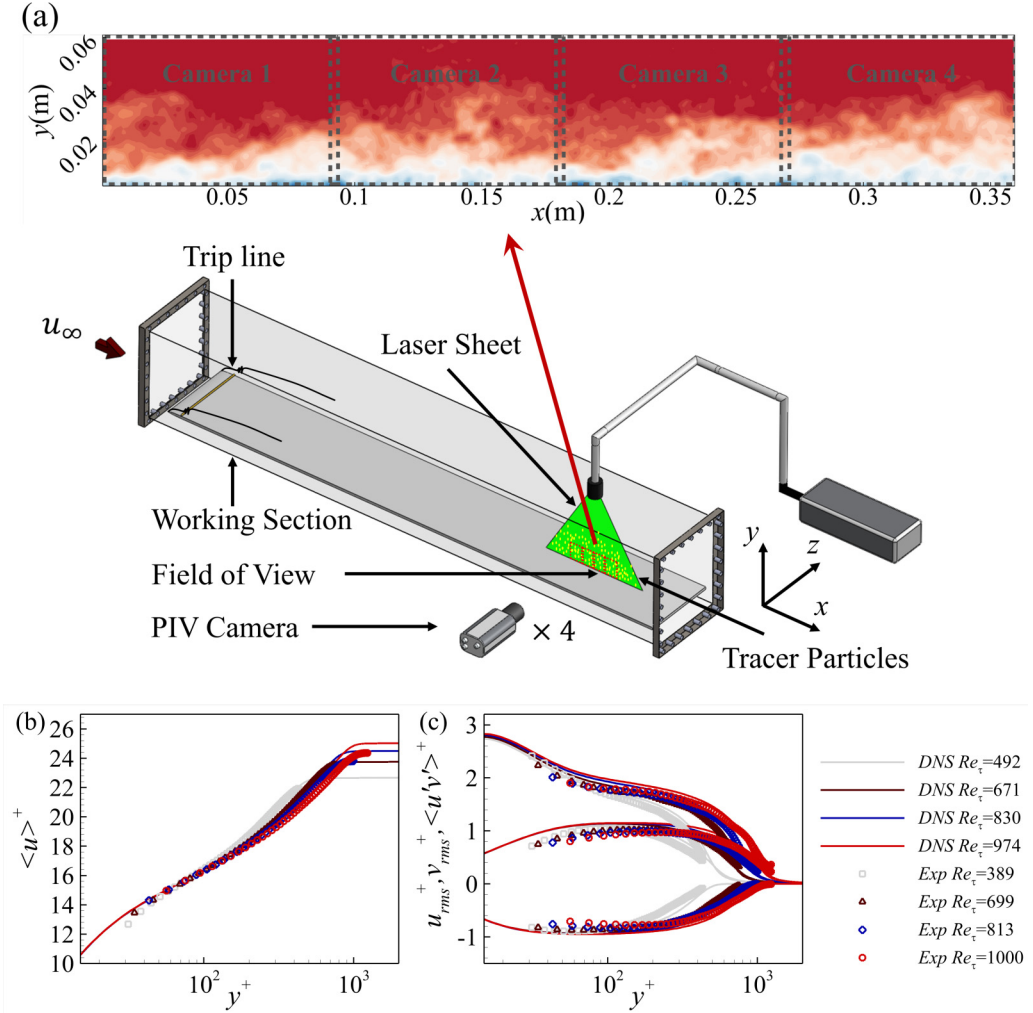
FIG. 1. (a) Schematic of experiments. (b) Mean streamwise velocity profiles. (c) Mean second-order statistic profiles. The direct numerical simulation (DNS) data are reported by Schlatter and Örlü [41].

and finally decreases as it approaches the edge of TBL. The two-point correlation of turbulent fluctuations has confirmed this trend [23,38]. This kind of spatial characteristic is to some extent independent of interface height conditions [23]. Whether there are more consistent outer-layer self-similar features based on the interface perspective needs further investigation.

There are few studies to explore the consistency of turbulence characteristics and turbulence structure in the wake region based on the T/NT interface perspective. The main work in this paper is to investigate the outer-layer self-similarity from the T/NT interface perspective. The first section gives the introduction. Section II describes the particle image velocimetry (PIV) experiment and the basic parameters. Section III is the results and discussion: Sec. III A discusses the detection of the T/NT interface and its statistical characteristics; Sec. III B introduces the interface-based triple velocity decomposition; Sec. III C reveals the outer-layer self-similarity of the raw velocity profile; Sec. III D discusses the outer-layer self-similarity of the spatial characteristics; and Sec. III E gives the outer-layer self-similarity of TKE based on the energy superposition effect. Section IV is the conclusion.

TABLE I. The basic parameters of experiments.

Case	Re_τ	u_τ (m/s)	u_∞ (m/s)	δ_{99} (m)	δ (m)	Sampling frequency (Hz)	Field of view, $x \times y$ (δ_{99}^2)	Spatial resolution of PIV (δ_{99}^2)
1	1000	0.019	0.467	0.048	0.058	800	7.4×1.2	0.019×0.019
2	813	0.016	0.374	0.048	0.060	600	7.4×1.2	0.019×0.019
3	699	0.011	0.268	0.052	0.068	400	6.9×1.1	0.017×0.017
4	389	0.006	0.137	0.054	0.069	200	6.6×1.1	0.017×0.017

II. EXPERIMENTAL SETUP

The experimental setup and database used in this paper have been reported in our previous work [39,40]. For integrity, the introduction of the experiments is still carefully described in this section. The experimental subject is the TBL at a low to moderate Reynolds number range. The PIV technique was used to measure the TBL. The experiments were conducted in the water tunnel at Tianjin University, the size of the working section of which is 4.2 m (length) $\times 0.6$ m (width) $\times 0.7$ m (height). The free-stream turbulent intensity of the water tunnel was $< 0.8\%$. The TBL is generated on an acrylic flat plate with dimensions of 4.0 m (length) $\times 0.6$ m (width) $\times 0.02$ m (thickness). The leading edge of the plate is elliptical (major axis : minor axis $= 10 : 1$) to ensure the flow entry above the plate. To avoid the influence of the boundary layer created by the water tunnel wall, the plate was placed 0.1 m away from the bottom wall. The 3-mm-diameter trip wire was placed 0.11 m downstream of the leading edge of the plate to induce the boundary layer transition. The experimental scheme is shown in Fig. 1(a). The DANTEC polyamide seeding particles (PSP-20) were used to display the motion of the flow. The average diameter of the tracer particles is 20 μm, and its density is 1.05 g/cm^3. The tracer particles were illuminated by the laser sheet with a thickness of 1 mm. The laser sheet was generated by a Litron LDY-304 high-speed laser with a pulse energy of 30 mJ.

The experiments used four high-speed complementary metal-oxide semiconductor cameras (1280×800 pixel^2), which were stitched together to form a large field of view and measured the TBL from the streamwise-wall-normal slice. The synchronized measurements of four cameras were ensured by a synchronizer. The size of the large field of view is 0.36×0.06 m^2. The sampling frequencies of the PIV are 800, 600, 400, and 200 Hz for the four different cases. Hence, the dimensionless time intervals between adjacent frames ($\Delta t^+ = \Delta t u_\tau^2 / \nu$) are 0.50, 0.46, 0.34, and 0.20. The friction Reynolds numbers ($Re_\tau = \delta_{99} u_\tau / \nu$) for cases 1–4 are 1000, 813, 699, and 389, respectively. The ν is the kinematic viscosity of water, u_τ is the friction velocity, and δ_{99} is the thickness of the TBL (defined by 99% free-stream velocity u_∞). The basic parameters of the experiments are given in Table I. The amount of particle images for a single acquisition limited by the camera memory is 8216 frames. Six acquisitions were completed to ensure sufficient data, and 8216×6 frames of particle images (8215×6 frame velocity fields) were obtained. To verify the accuracy of the PIV data, the statistical results of the experimental data are compared with direct numerical simulation (DNS) data reported by Schlatter and Örlü [41]. As shown in Figs. 1(b) and 1(c), the one-point statistics of experimental data are in good conformity compared with that of the DNS data.

III. RESULT AND DISCUSSION

A. T/NT interface

The T/NT interface is a conceptual interface that describes the spatial boundary between the turbulent and non-turbulent components [1]. The turbulent flow shows significantly different physical characteristics than the flow in the non-turbulent region. Therefore, the detection of the T/NT interface must be based on the physical quantities (such as velocity and vorticity) which are
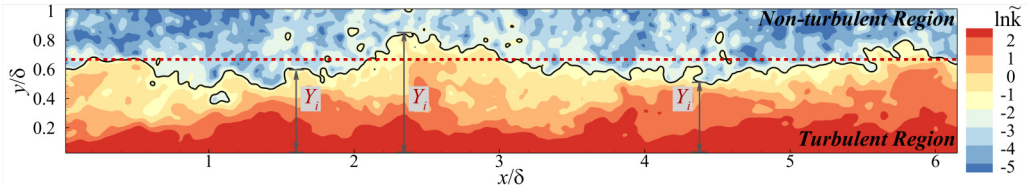
FIG. 2. Instantaneous snapshot of the turbulent/non-turbulent (T/NT) interface: T/NT interface (black solid line), mean interface height (red dashed line), and definition of interface height (dark gray solid line with double arrow).

significantly different on both sides of the T/NT interface [33,34,36]. The T/NT interface detection methods reported previously include (i) vorticity or vorticity-based method [27,34,36,42–48]; (ii) velocity and velocity-based method [30,49–51]; (iii) passive scalar [51–53]; (iv) TKE [20,21,38,54,55]; and (v) other methods [56–59]. For different flows, such as TBL, jet, mixing layer, etc., interface detection encounters different difficulties [51]. For example, for the TBL, the background noise is greater than the background of the jet. The database from the experimental measurement or numerical simulation should also be considered [57]. Compared with the DNS, the inevitable background noise of the water tunnel makes it difficult to detect the continuous interface based on the vorticity method [51,57]. In addition, the PIV algorithm relies on the query window, which leads to the inability to accurately resolve a small velocity gradient [51]. For the PIV database of TBLs, the vorticity-based interface detection methods are difficult to pursue. In this paper, the focus is on the self-similarity behavior in the outer layer from the T/NT interface perspective. It is important to capture the continuous high and low T/NT interface in the outer intermittent region. The entrainment motion near the T/NT interface is not the subject of discussion. Accurate detection of the complex features (such as the viscous nibbling motion) of the T/NT interface is not required. The T/NT interface is judged to be high or low by comparing with its mean value, and this expression will be used in subsequent sections. The T/NT interface detection is based on the local TKE (L-TKE) which was proposed by Chauhan *et al.* [21]. The L-TKE is shown below:

$$\tilde{k} = \frac{100}{9u_\infty^2} \sum_{m,n=-1}^{1} [(\tilde{u}_{m,n} - u_\infty)^2 + (\tilde{v}_{m,n})^2]. \tag{1}$$

Compared with the flow in the non-turbulent region, the velocity is smaller than the free-stream velocity u_∞, which means that $\tilde{k}$ is larger in the turbulent region. Hence, the T/NT interface can be found based on the $\tilde{k}$ according to a suitable threshold $\tilde{k}_{\text{th}}$. To obtain $\tilde{k}_{\text{th}}$, it is necessary to consider that the distribution of the intermittent factor (γ) in the outer region is Gaussian distribution [1]. The instantaneous height (Y_i) of the T/NT interface also follows this distribution. In three-dimensional physical space, the interface is distorted and multivalued due to the entrainment motion [18]. The instantaneous interface height is defined as the lower envelope of the T/NT interface [21]. In the L-TKE method, a suitable threshold $\tilde{k}_{\text{th}}$ should satisfy two criteria. The first is that $E(Y_i) + 3\sigma(Y_i) \approx \delta$, where $E(Y_i)$ is the expectation, and $\sigma(Y_i)$ is the standard deviation of Y_i. This is because the turbulent region cannot extend beyond the TBL. Second, the distribution of Y_i should be consistent with the Gaussian distribution, and it should also be consistent with the distribution of the intermittent factor γ. Here, δ is the true boundary layer thickness which is obtained based on the composite velocity profile [60]. Also, δ includes the entire outer-layer intermittent region, so it is larger than δ_{99}, which is defined based on $0.99u_\infty$.

According to these two criteria, the thresholds of $\tilde{k}$ for cases 1–4 are obtained as $\tilde{k}_{\text{th1}} = 0.157$, $\tilde{k}_{\text{th2}} = 0.082$, $\tilde{k}_{\text{th3}} = 0.111$, and $\tilde{k}_{\text{th4}} = 0.100$, respectively. The instantaneous snapshot of the T/NT interface is shown in Fig. 2. The solid black line is the slice of the T/NT interface in the streamwise-wall-normal plane. The region above the T/NT interface is the non-turbulent region with a smaller $\tilde{k}$, while the counterpart below the T/NT interface is the turbulent region with a relatively larger

TABLE II. The statistics of the T/NT interface height.

Case	Re_τ	$\frac{E(Y_i)}{\delta}$	$\frac{\sigma(Y_i)}{\delta}$	$\frac{\sigma(Y_i)}{E(Y_i)}$	$\frac{E(Y_i)}{\delta_{99}}$	$\frac{\sigma(Y_i)}{\delta_{99}}$
Corrsin and Kistler [1]	<2000	–	–	0.20	0.80	0.16
Semin *et al.* [61]	600	–	–	0.15	0.60	0.09
Chauhan *et al.* [21]	2700–22000	0.64–0.67	0.11–0.13	0.16–0.2	–	–
Chauhan *et al.* [21]	14 500	0.67	0.11	0.167	–	–
Eisma *et al.* [62]	2053	–	–	0.20	0.90	0.18
Wu *et al.* [20]	483	0.67	0.13	0.19	0.82	0.16
This paper (Case 1)	1000	0.67	0.11	0.164	0.80	0.14
This paper (Case 2)	813	0.67	0.11	0.171	0.82	0.14
This paper (Case 3)	699	0.67	0.11	0.168	0.87	0.15
This paper (Case 4)	389	0.67	0.13	0.200	0.85	0.17

$\tilde{k}$. The T/NT interface has an obvious waviness around its mean value (red dashed line in Fig. 2), showing the intermittency of the outer region of the TBL. The local instantaneous interface height is indicated by the dark gray solid line with double arrow in Fig. 2.

The statistics of the T/NT interface are given in Table II, and the corresponding results from previous literature are also given for comparison. The expectation of the T/NT interface is 0.67δ, and the standard deviation is 0.11δ–0.13δ for all four cases. Figure 3 displays the statistical distribution characteristics of the T/NT interface. As shown in Fig. 3(a), the probability density function of the T/NT interface height is close to the Gaussian distribution for all four cases. The cumulative distribution function of the T/NT interface height corresponds to the distribution of the intermittency factor (γ). This indicates that the T/NT interface detected by the L-TKE detection method can reflect the intermittency in the outer region of the TBL.

B. Interface-based triple velocity decomposition

The traditional velocity decomposition technique (Reynolds decomposition) is to decompose the raw velocity into its ensemble mean and its fluctuations [63]. For studies not interested in outer region intermittency, Reynolds decomposition is available in the fully turbulent region, but it causes turbulent fluctuations to be overestimated in the outer-layer intermittent region [38]. Thus, the Reynolds decomposition fluctuations would induce misleading results. For example, in
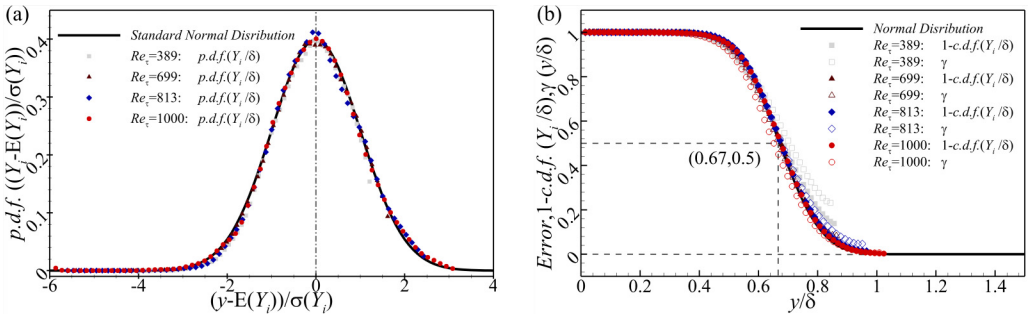

FIG. 3. Statistical distribution characteristics of the turbulent/non-turbulent (T/NT) interface. (a) Probability density function of the T/NT interface height. (b) Cumulative distribution function of the T/NT interface height and the distribution of intermittent factor. Gaussian distribution (black solid line). Case 1: Red circles, ● and ○; Case 2: blue diamonds, ◆ and ◇; Case 3: brown deltas, ▲ and △; and Case 4: bright gray squares, ▪ and □.
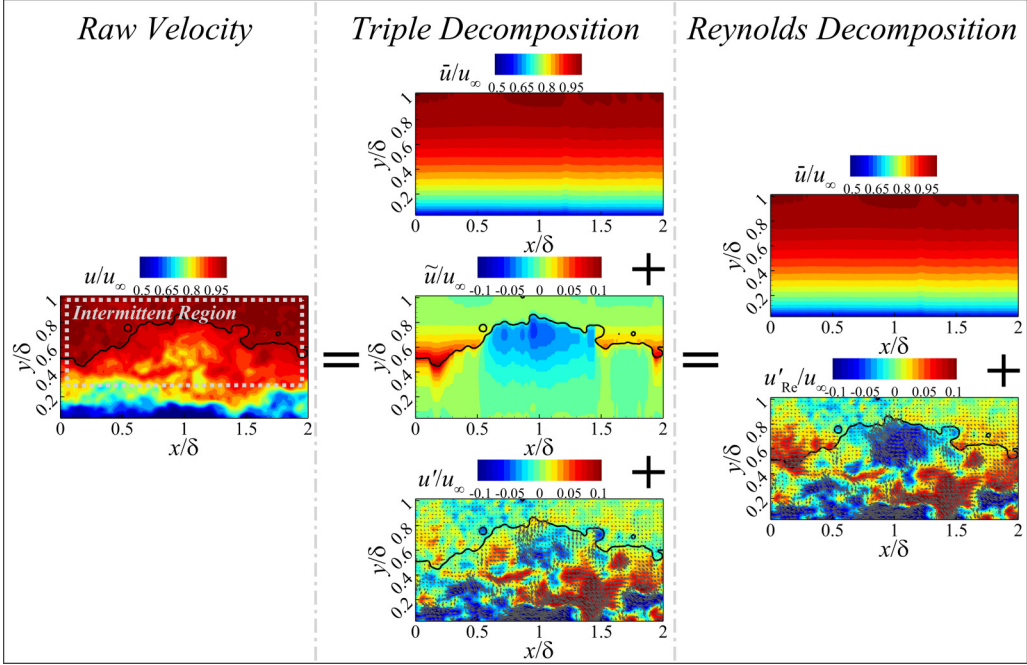
FIG. 4. Velocity decomposition displayed in a snapshot. Left column: Raw velocity; middle column: triple velocity decomposition; and right column: Reynolds decomposition for comparison.

the intermittent region, the correlation of turbulent fluctuations can be extended to a larger extent in the flow field [38]. Researchers considered this in a previous study [64]. It was not until the development of hot-wire technology that it became possible to use conditional averaging based on intermittency [17,65]. For the special problem, introducing a triple decomposition of the raw velocity to highlight the local turbulent structure is a possible technique [66]. When intermittency is included, the transition of the signal between turbulent and non-turbulent states must be considered [22,27,38]. Thus, it is important to decompose the raw velocity based on the T/NT interface. The triple decomposition was introduced in our previous work [23]. The triple decomposition method is to decompose the raw velocity into the ensemble average ($\bar{u}$), the interface-based conditional average ($\tilde{u}$), and the fluctuation (u'). It can be written as

$$u(x, y, t) = \bar{u}(x, y) + \tilde{u}(y, Y_i) + u'(x, y, t), \tag{2}$$

$$v(x, y, t) = \bar{v}(x, y) + \tilde{v}(y, Y_i) + v'(x, y, t), \tag{3}$$

where $\bar{u}$ is only related to the spatial location (x, y), $\tilde{u}$ is only related to the T/NT interface height Y_i and the wall-normal coordinate y, and t is the time. The result of decomposition is shown in Fig. 4, and the Reynolds decomposition result is also displayed for comparison. The left column is the raw velocity, where the T/NT interface is distributed in the intermittent region. The middle column is the triple velocity decomposition. Here, $\tilde{u}$ has a significant difference in the outer region for different interface heights. For the high interface, $\tilde{u}$ is negative below the T/NT interface, and it is positive around the low interface, especially in the non-turbulent region. Near the wall, $\tilde{u}$ is close to zero, which means that the influence of intermittency is not obvious at here. The turbulent fluctuations are significantly different than the Reynolds decomposition fluctuations in the right column. The Reynolds decomposition fluctuations are not negligible in the non-turbulent region when the T/NT interface is low, and in the turbulent bulge, the negative fluctuations are exaggerated.
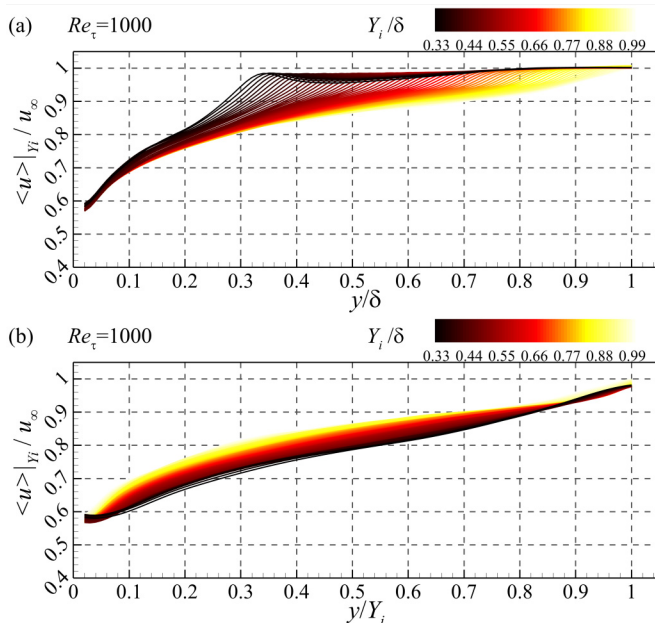
FIG. 5. Conditional raw velocity profile based on different interface height for the Case 1 ($Re_\tau = 1000$). The line color from black to yellow corresponds to the low- to high-interface condition. (a) Dimensionless based on the boundary layer thickness δ. (b) Dimensionless based on the turbulent/non-turbulent (T/NT) interface height Y_i. The range of the T/NT interface height is $0.33\delta \leqslant Y_i \leqslant 1.00\delta$.

Both are effectively avoided in triple decomposition fluctuations. The following discussion is based on the triple decomposition fluctuations.

C. Interface-based velocity self-similarity

Interface-based conditional statistics reveal to the distribution of physical statistics in the outer-layer intermittent region from the T/NT interface perspective. As the database has sufficient samples, the convergence of the conditional mean raw velocity is guaranteed at all interface heights. The validation of the convergence is discussed in detail in the Appendix.

The conditional mean streamwise raw velocity is shown in Fig. 5. The color of the solid line from black to yellow represents the different T/NT interface heights from low to high interface. According to the analysis in Sec. III A, the range of interface heights is $0.33\delta \leqslant Y_i \leqslant 1.00\delta$. The dimensionless approach in Fig. 5(a) is based on the overall boundary layer thickness δ introduced in Sec. III A. In the logarithmic region and below, the conditional mean velocity profiles are insensitive to interface height conditions. This reveals that the fluctuation of the T/NT interface does not have a significant effect on the logarithmic region and the region below it. The viscous effect cannot be ignored here [8–10]. In the outer region, the difference in the conditional raw velocity profile becomes gradually more apparent. Then the interface-based entrainment motion is in the near interface region. It is relatively independent of the main part of the wake region in terms of physical mechanism. The viscosity is also non-negligible near the interface [18,21]. In this paper, we focus on the region between the two above where the inertial force is dominant [16]. For the low-interface condition, the raw velocity reaches the free-stream velocity u_∞ at a lower wall-normal height, indicating a stronger shear effect. The opposite result is observed for the high-interface condition. This is due to the statistical results that the low interface corresponds to the high-speed structure, while on the contrary, the low-speed structures are below the high interface [23,27]. As shown in Fig. 5(a),
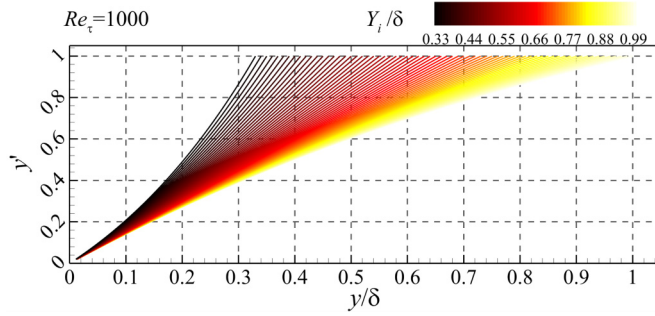
FIG. 6. Exponential wall-normal coordinate self-similarity relation f_{Y_i}. The line color corresponds to the turbulent/non-turbulent (T/NT) interface height.

it is worth considering that the shape of the conditional raw velocity profile shows a clear self-similarity in the turbulent region. If this assumption exists, the self-similarity relationship could be expressed as $\langle u \rangle |_{Y_i} = F[f_{Y_i}(y)]$ for the different interface conditions. First, the T/NT interface height condition is the primary consideration. In Fig. 5(b), the dimensionless method based on the T/NT interface height is used. The interface-based dimensionless method allows the wall and the T/NT interface position to be standardized as 0 and 1. The conditional statistics for regions near the interface are consistent. This phenomenon proves the relative independence of the region near the interface. However, there are significant differences between the high- and low-interface conditions in the outer region far enough away from the interface. This suggests that the self-similarity of the raw velocity profile is different along the wall-normal direction for different interface conditions. It is not a crude linear extension and compression based on the local T/NT interface height. Therefore, the self-similarity of the streamwise velocity profile should not only consider the T/NT interface height but should also be the function of the wall-normal coordinates. The exponential wall-normal coordinate self-similarity relation f_{Y_i} based on the transformation factor is given in Eqs. (4)–(6). In Eq. (4), y' is the wall-normal coordinate transformed by the self-similarity relation:

$$y' = f_{Y_i}(y) = \frac{y}{Y_i} \exp[\eta_{Y_i}(y)], \tag{4}$$

$$\eta_{Y_i}(y) = \frac{Y_i - y}{Y_i - y_{\log}} \psi_{Y_i}, \tag{5}$$

$$\psi_{Y_i} = \frac{Y_i}{\delta} - E\left(\frac{Y_i}{\delta}\right). \tag{6}$$

The transformation factor $\eta_{Y_i}(y)$ introduced in Eq. (5) is the function of the wall-normal coordinate y. The construction of $\eta_{Y_i}(y)$ is based on the T/NT interface height and the wall-normal variation. Firstly, the left-hand-side fractional formula in Eq. (5) expresses the ratio of the distance from the wall-normal position to the interface $Y_i - y$ and the distance from the upper boundary of the logarithmic region to the interface $Y_i - y_{\log}$. The upper boundary of the logarithmic region is defined as $0.15\delta_{99}$ [11], that is, $y_{\log} = 0.15\delta_{99}$. The ratio considers the wall-normal variation of the self-similarity. Then the right-hand-side ψ_{Y_i} gives the adjustment factor. The definition of ψ_{Y_i} is given in Eq. (6). Here, ψ_{Y_i} is related to how much the interface height is offset from its mean value. The mean value of the interface height is $2\delta/3$ obtained in Sec. IIIA [$E(Y_i) = 0.67\delta$]. This is because, as shown in Fig. 5(b), the difference in the raw velocity profile is obvious as the interface height departs further from its mean value. The exponential self-similarity relation f_{Y_i} is given in Fig. 6.

As shown in Fig. 7, the distribution of the raw velocity profile is shown in the frame of y', and the corresponding results in the y/Y_i coordinate are given for comparison. It shows good agreement
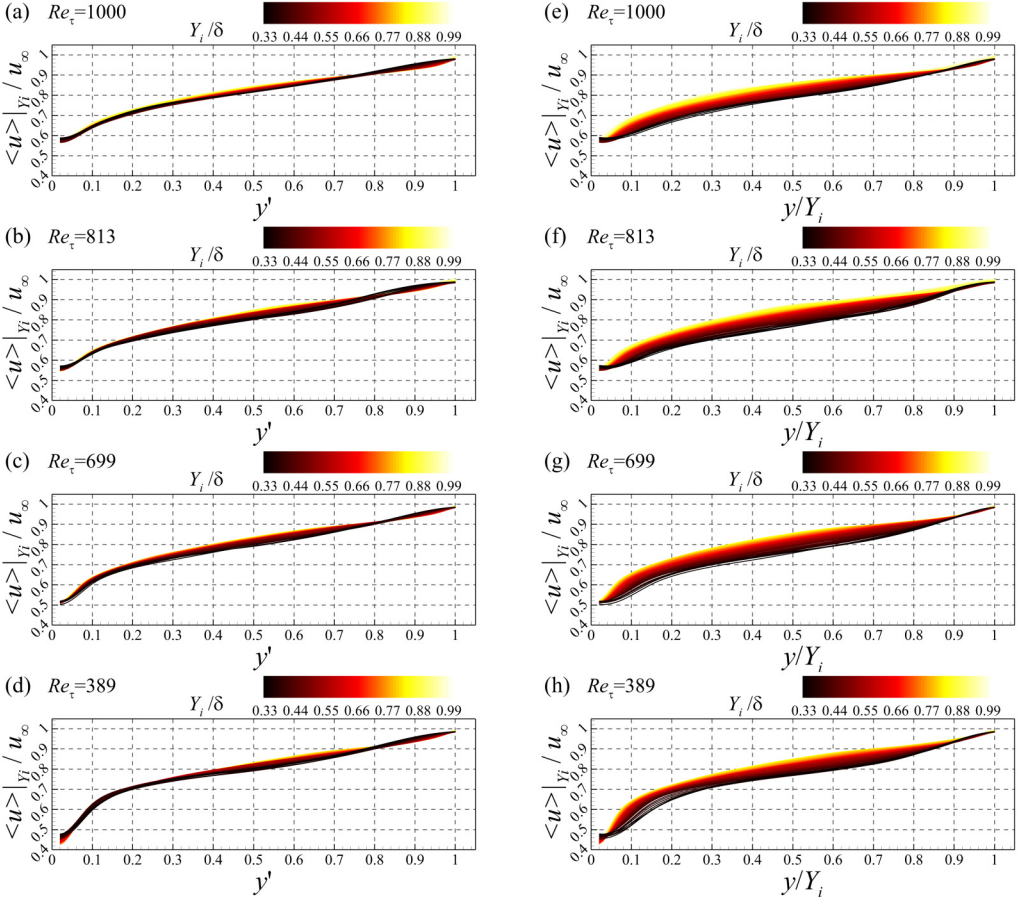
FIG. 7. Conditional raw velocity profile in the frame of y' and y/Y_i based on different interface heights. The line color corresponds to the turbulent/non-turbulent (T/NT) interface height.

for all interface conditions. This indicates that the raw velocity profiles exhibit the exponential self-similarity in the outer region according to the T/NT interface coordinate. For cases 3 and 4, due to the limitation of the wall-normal size of the field of view, few overheight interfaces are not captured. Therefore, they are not shown in Fig. 7. Only the captured T/NT interface is discussed in this paper.

In Fig. 5(a), the velocity profile shows an inflection point close to the T/NT interface position. The appearance of inflection points indicates strong shear near the interface and non-negligible viscosity. The region on the right side of the inflection point is the near interface region. In the region close to the T/NT interface, some coherent vortices can be observed [23]. The velocity gradient increases because the coherent vortex is preferentially aligned with the interface [31]. Figures 7(e)–7(h) also reveal that the results in this region do not respond to the differences of local interface height, which suggests that the region close to the interface is also somewhat unaffected by the interface condition. The scale from the inflection point to the T/NT interface is defined to express the scale of the region influenced by the T/NT interface. As shown in Fig. 8(a), the red double arrows indicate the near-interface region. The distribution of this scale for the different T/NT interface conditions is displayed in Fig. 8(b). The scale is generally consistent for different interface conditions, and its mean is 0.09δ. To ensure the reliability of the results, the positions of the inflection points
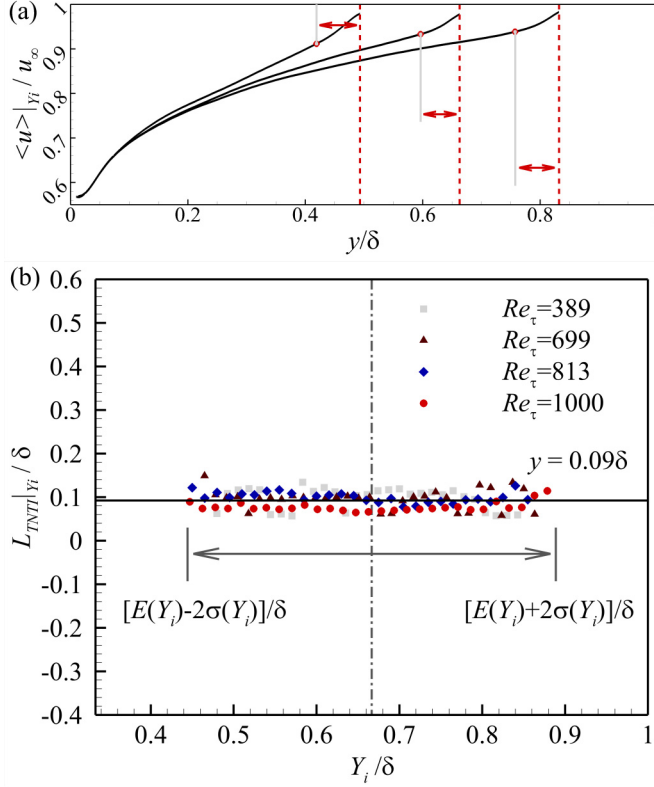
FIG. 8. (a) Definition of the scale of the region affected by the interface. The interface height for the representative velocity profiles is $\delta/2$, $2\delta/3$, $5\delta/6$. The red circles point out the location of the inflection points. (b) Scale of the region affected by the interface. Case 1: Red circles ●; Case 2: blue diamonds ◆ Case 3: brown deltas ▲; and Case 4: bright gray squares ■.

are given when the T/NT interface height is $\{[E(Y_i) - 2\sigma(Y_i)]/\delta, [E(Y_i) + 2\sigma(Y_i)]/\delta\}$. The results are aimed at separating the region dominated by the interface in the subsequent parts.

D. Interface-based spatial characteristics self-similarity

This part is set up to discuss the self-similarity of the spatial features of the outer-layer structure from the T/NT interface perspective. The two-point correlation function is used to display the spatial characteristics of the outer-layer structure, which is shown in Fig. 9. The two-point correlation function is expressed as

$$R_{u'u'}|_{Y_i}(\Delta x, y, y_{\text{ref}}) = \frac{\langle u'|_{Y_i}(x_{Y_i}, y_{\text{ref}})u'|_{Y_i}(x_{Y_i} + \Delta x, y)\rangle}{\sqrt{\langle[u'|_{Y_i}(x_{Y_i}, y_{\text{ref}})]^2\rangle}\sqrt{\langle[u'|_{Y_i}(x_{Y_i} + \Delta x, y)]^2\rangle}}. \tag{7}$$

The turbulent fluctuations are based on the triple velocity decomposition in Sec. III B. The contours represent the region with correlation coefficients >0.5. In Fig. 9(a), the slices show the contours of the correlation coefficients for a certain interface height condition. The slices are arranged in the direction of the interface height Y_i/δ. The two-point correlation preserves the original spatial framework of the flow field and gives the results at the corresponding reference height according to the exponential self-similarity relation. The spatial characteristics of the outer-layer structures
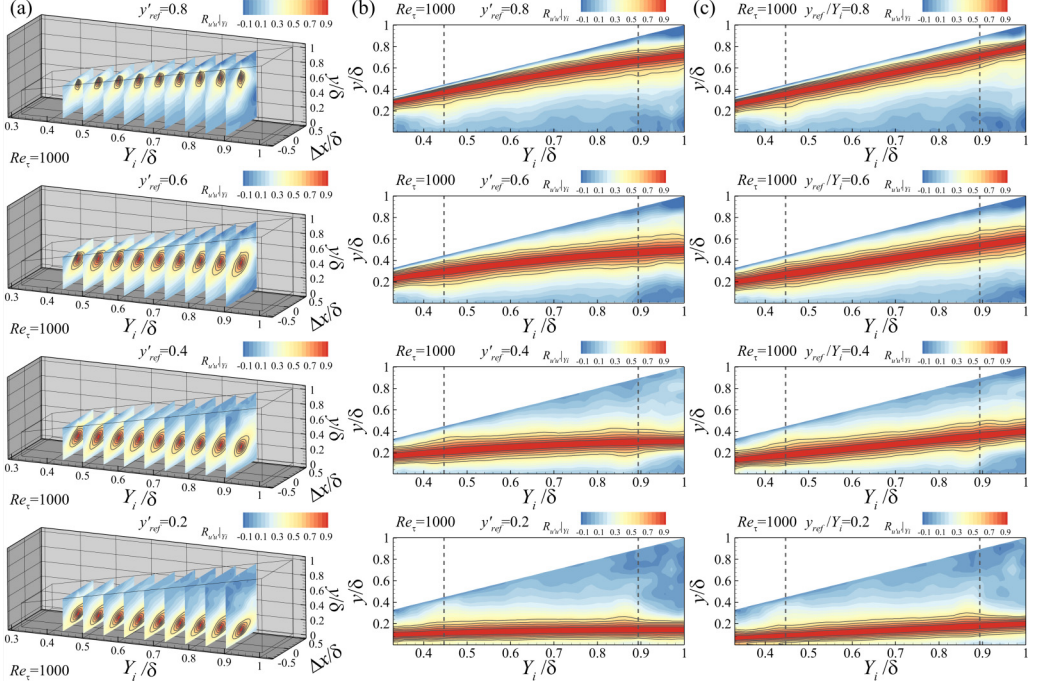
FIG. 9. (a) Two-point correlation of turbulent fluctuations for different interface conditions. (b) Cross-section of two-point correlation results ($\Delta x/\delta = 0$). The reference height $y'_{\rm ref}$ is based on the exponential self-similarity relation. (c) Corresponding results normalized by the local interface heights. The dark gray dashed line is the range $\{[E(Y_i) - 2\sigma(Y_i)]/\delta, [E(Y_i) + 2\sigma(Y_i)]/\delta\}$.

are self-similar at the corresponding reference heights. At lower reference heights ($y'_{\rm ref} = 0.2$), the elliptic contours of the two-point correlation function show an inclined tendency due to the shear effect within the TBL. For the middle two reference heights, the wall-normal scale of the contour is larger than the reference heights close to the wall as well as close to the interface. The inclined characteristics of the elliptical contours decrease which indicates the reduction of shear. At reference heights close to the interface, the range of contours is smaller than the middle two which suggests a decreasing trend of the wall-normal scale. Figure 9(b) is the corresponding cross-section ($\Delta x/\delta = 0$) of Fig. 9(a). For the convergence, only results with interface heights in the range $\{[E(Y_i) - 2\sigma(Y_i)]/\delta, [E(Y_i) + 2\sigma(Y_i)]/\delta\}$ are discussed. It is demonstrated in the Appendix that turbulent-fluctuation-based statistics are convergent in this range. The dark gray dashed lines indicate the range of reliable results. For different interface conditions, the wall-normal scale of the contours is well preserved at the corresponding reference height. The wall-normal scale of the contours S_y is defined as the wall-normal scale of the elliptic correlation coefficient contours which is equal to 0.5 at $\Delta x = 0$. This reveals good agreement in the wall-normal scale of the structures for a certain reference height. In Fig. 9(c), the reference heights are normalized by the local interface heights. Compared with Fig. 9(b), the results in Fig. 9(c) are a linear correspondence. It fails to establish the nonlinear relationship according to the streamwise raw velocity in Sec. III C.

Figure 10 shows the distribution of the wall-normal scale at different reference heights. The interface-based velocity decomposition eliminates the amplification of turbulent fluctuations in the outer-layer region of the traditional Reynolds decomposition. The wall-normal scale increases along the wall-normal direction and reaches its maximum, then decreases as it approaches the T/NT interface. This trend is consistent with previously reported research. According to Townsend's [67] attached eddy hypothesis, the scale of the structure increases with the height from the wall in the
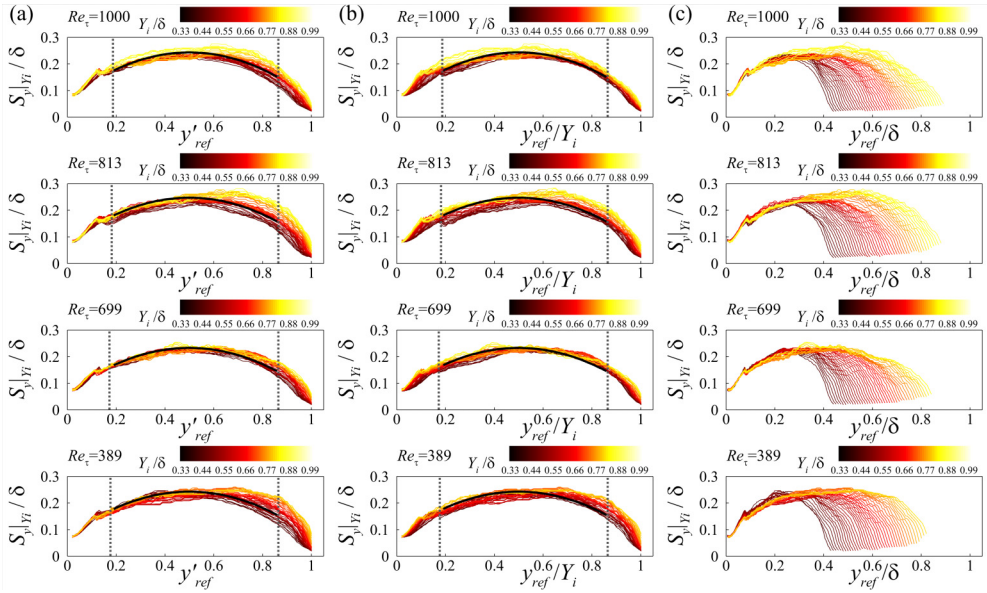
FIG. 10. The wall-normal scale of the outer-layer structure according to the correlation coefficient >0.5. The line color corresponds to the reference height. The black solid line represents the fitted curve $\widetilde{S}_y/\delta$.

logarithmic region. As the height from the wall increases, the number of detached eddies begin to increase, and the outer-layer intermittency begins to appear. The scale of the turbulent structure gradually deviates and loses the scaling based on the attached eddy model [68] above the logarithmic region [67]. Before reaching its maximum, the scale of the structure continues to increase as its height from the wall increases in the wake region [37]. Near the interface, the characteristic scale of the structure is on the order of the Taylor microscale [31]. Kwon *et al.* [38] discussed the difference in the two-point correlation between different decomposition methods. The two-point correlation of Reynolds fluctuations shows the outer-layer structural spatial characteristics in the outer intermittent region are overestimated [38]. Previous literature demonstrates the justification of the present results and provides the explanation from the structural perspective. This motivates that the wall-normal scale of the outer-layer structure is not only related to the height from the wall but also related to the distance from the T/NT interface. Figure 10(a) shows the results in the self-similarity framework, Fig. 10(b) shows the results normalized by the local interface height, and Fig. 10(c) shows the results normalized by the boundary layer thickness. As Figs. 10(a) and 10(b), S_y shows self-similarity under different interface height conditions. Compared with the violent linear stretching in Fig. 10(b), the results under the self-similar framework are more consistent on the near-wall side. On the side close to the interface, the results of linear stretching are better. Despite the differences, they all reveal the self-similar wall-normal scale distribution trend for different interface conditions. The quadratic functions $\widetilde{S}_y/\delta = a_1 y'(1-y') + b_1$ and $\widetilde{S}_y/\delta = a_2 y/Y_i(1-y/Y_i) + b_2$ are used to fit this variation trend. The quadratic functions are only used here to model the trend of the wall-normal scale. The fitted quadratic curve is shown as the solid black line in Fig. 10. The coefficients for cases 1–4 are consistent. The coefficient a is 0.70 ± 0.02 and b is 0.07 ± 0.01. The difference between the fitted coefficients in the two frameworks is small. This further emphasizes the self-similarity of the spatial characteristics of the outer-layer structures at the low to moderate Reynolds number range. The logarithmic region and below and the near-interface region identified in Sec. III C are not the regions in which the viscosity can be ignored. Therefore, the inertial dominated range is indicated by the dark gray dashed lines in Fig. 10. The self-similar spatial characteristics of the outer-layer structures play a role in the subsequent discussion.
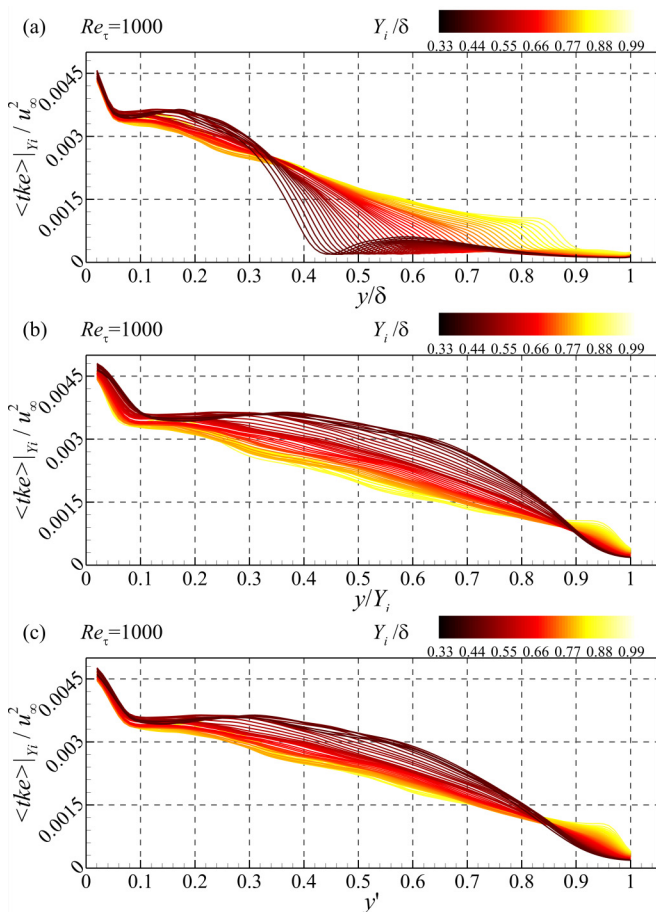
FIG. 11. (a) Turbulent kinetic energy (TKE) profile for different interface conditions. (b) TKE profile removing the logarithmic region and below and the region influenced by the turbulent/non-turbulent (T/NT) interface. The line color corresponds to the T/NT interface height.

E. Interface-based turbulent kinetic energy self-similarity

In this part, the baton of Secs. III C and III D is picked up. The self-similarity of TKE based on the T/NT interface is investigated. The TKE is defined as tke $= (u'^2 + v'^2)/2$, where u' and v' are the interface-based turbulent fluctuations introduced in Sec. III B. The distribution of TKE along the wall-normal direction based on the different dimensionless methods is given in Fig. 11. The Gaussian distribution of the T/NT interface leads to the non-convergent curve of TKE at extreme interface conditions. Hence, the interface-based conditional statistics are displayed in $\{[E(Y_i) - 2\sigma(Y_i)]/\delta, [E(Y_i) + 2\sigma(Y_i)]/\delta\}$. The convergence validation of the experimental data is discussed in the Appendix. In Fig. 11(a), the normalized method is based on the thickness of the TBL. There is little difference for the TKE in the logarithmic region and below. This once again verifies that the turbulence characteristics near the wall are not obviously connected to the T/NT interface. In the wake region, the conditional mean TKE begins to respond to interface-based conditional statistics. The TKE is maintained in the wall-normal direction for the low-interface conditions compared with that for the high-interface conditions. This indicates that the TKE is higher in the turbulent region if the interface height is lower, but it calculates both turbulent and non-turbulent components. Figure 11(b) shows interface-based dimensionless methods which

defines the wall position as 0 and the interface position as 1. It reveals the correspondence of turbulent characteristics throughout the turbulent region. The above energy distribution features are shown more clearly, but this approach is a kind of violent linear stretching of wall-normal coordinate y. In Fig. 11(c), the distribution of the TKE is given under the nonlinear self-similarity framework in which the conditional mean velocity is self-similar. The high-energy characteristics of the low-interface conditions still exist. This means that the self-similarity of TKE needs further consideration.

The static pressure of the turbulent bulge is greater than the background pressure when the interface is higher, and conversely, the interface is lower when the static pressure in the turbulent region is lower than the background pressure [22]. It is hypothesized that this phenomenon arises due to the spatially limited turbulent region and the superposition effect of turbulent structures in the outer-layer intermittent region. The hairpin vortex packets in the logarithmic region enter the wake region and form turbulent lumps with a superimposed structural arrangement as the vortex packet structure evolves. This interface-based energy superposition effect should be more pronounced above the logarithmic region. The effect is more obvious as the distance from the upper boundary of the logarithmic region increases. At the same time, the energy superposition effect should fade away approaching the T/NT interface. Based on the ideas in Sec. III C, the logarithmic region and below and the region close to the interface are not part of the current discussion. Because of that, they will not be considered.

The energy superposition effect leads to the reconsideration of TKE. The TKE at the corresponding reference height should involve the corresponding wall-normal range which is defined by the two-point correlation. Hidden behind the energy superposition effect, the energy of the outer-layer structures at the corresponding heights is self-similar for different interface conditions. According to Sec. III D, the local overlaps are defined. The number of local overlaps N_{Y_i} is the count of the overlaps of two-point correlation contours which is > 0.5. It characterizes the superposition degree of the two-point correlation function of the turbulent fluctuations at the current reference height. Then the reconsideration of the TKE at a certain reference height should involve the correlated wall-normal range defined by the two-point correlation function. Based on the energy superimposed concept, the reconsidered TKE can be written as

$$\langle \text{tke}^* \rangle |_{Y_i}(y') = \left[\sum_{\Omega_y|_{Y_i}(y')} \frac{\langle \text{tke} \rangle |_{Y_i}(s')}{N_{Y_i}(s')} \right] \exp[\xi_{Y_i}(y')], \tag{8}$$

$$\xi_{Y_i}(y') = \frac{\psi_{Y_i} \epsilon_{\log}^{Y_i}}{S_y(y')/Y_i}, \tag{9}$$

$$\epsilon_{\log}^{Y_i} = \frac{[Y_i - y(y')][y(y') - y_{\log}]}{[Y_i - y_{\log}]^2}. \tag{10}$$

In Eq. (8), the structural overlap is used to express the energy superposition effect. The conditional mean profile of the TKE, $\langle \text{tke} \rangle |_{Y_i}$, is divided by the local overlap N_{Y_i} at the corresponding position. Then the divided energy is accumulated in the range defined by two-point correlation $\Omega_y|_{Y_i}$. Here, $\Omega_y|_{Y_i}$ is the wall-normal range in which the two-point correlation coefficient is > 0.5 at $\Delta x = 0$. Secondly, the superposition effect of the TKE should consider its local interface height. The distances to the upper boundary of the logarithmic region and the interface should also be considered. These result in the energy superposition coefficient $\xi_{Y_i}(y')$, given in Eq. (9). In Eq. (9), ψ_{Y_i} defined in Eq. (6) is to express the deviation of the interface height from its mean value. The low interface leads to the superposition effect ($\psi_{Y_i} < 0$), but for the high-interface condition, the superposition effect is weaker ($\psi_{Y_i} > 0$). The denominator $S_y(y')/Y_i$ is the structural scale of the current reference height. Here, $\epsilon_{\log}^{Y_i}$ is to introduce the distances from the current reference height
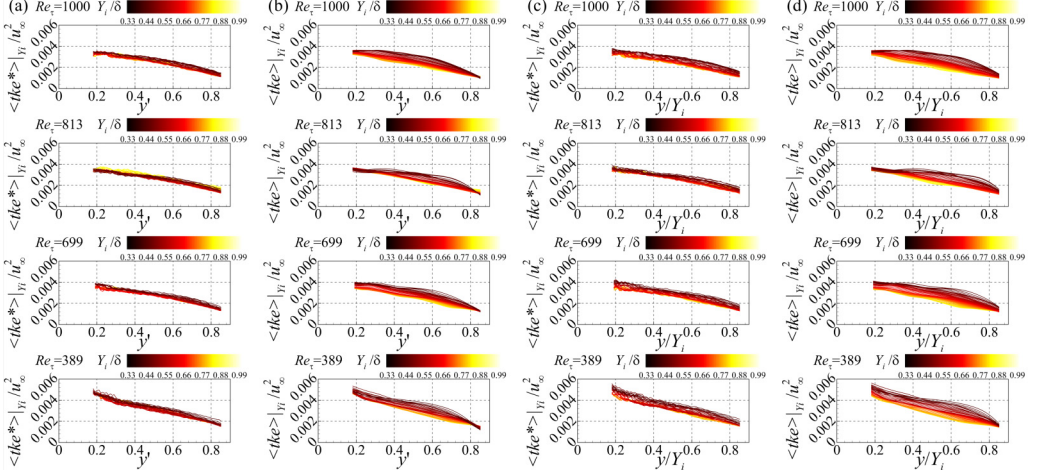
FIG. 12. (a) and (b) $\langle \text{tke}^* \rangle|_{Y_i}$ and $\langle \text{tke} \rangle|_{Y_i}$ under self-similarity framework for cases 1–4. (c) and (d) Corresponding results under y/Y_i framework for comparing. The line color corresponds to the turbulent/non-turbulent (T/NT) interface height.

to the interface and the upper boundary of the logarithmic region. The definition of $\epsilon_{\log}^{Y_i}$ is given in Eq. (10).

As shown in the Fig. 12, the reconsidered TKE, $\langle \text{tke}^* \rangle|_{Y_i}$, has been displayed under the y' [Fig. 12(a)] and y/Y_i [Fig. 12(c)] frameworks for the four cases. The same algorithm is used for the results of the local interface height dimensionless framework. The original conditional statistics of TKE, $\langle \text{tke} \rangle|_{Y_i}$, are also presented in Figs. 12(b) and 12(d) for comparison. The logarithmic region and below, as well as the region close to the interface, are excluded from the discussion. Therefore, these two regions are not presented here. Compared with $\langle \text{tke} \rangle|_{Y_i}$, the differences in TKE based on the interface height conditions are dismissed in the Figs. 12(a) and 12(c). In these two kinds of frameworks, the reconsidered TKE based on the energy superposition effect presents a consistent distribution. The consistency of the results under the self-similarity framework is better. This suggests that the self-similarity framework better reveals the self-similar behavior of TKE. It verifies the energy superposition effect based on the spatial structural characterization from the experimental database.

IV. CONCLUSIONS

From the perspective of the T/NT interface, the outer-layer self-similarity in turbulent characteristics is investigated from three aspects: the raw velocity, the spatial configuration characteristics of the structures, and TKE based on the energy superposition effect.

The database underpinning the results is the TBL experimental data obtained by PIV at the low to moderate Reynolds number range. The large field of view stitched by four cameras makes this paper possible. The main idea in this paper is to reveal the outer-layer self-similarity from the perspective based on the T/NT interface. The L-TKE criterion is used to detect the T/NT interface. The statistical characteristics of the T/NT interface height are investigated at low to moderate Reynolds number range ($\text{Re}_\tau = 389–1000$). The normal fluctuation of the interface in the intermittent region results in the normal distribution of the interface height. The intermittency in the outer region prompts the consideration of velocity decomposition methods according to the fluctuation of the T/NT interface. The triple velocity decomposition with the middle interface-based components $\tilde{u}(y, Y_i)$ and $\tilde{v}(y, Y_i)$ is introduced. The turbulent fluctuations introduced by the interface-based velocity decomposition

ensure that the statistical results are not misguided by the traditional Reynolds decomposition in the intermittent region.

The interface-based conditional raw streamwise velocity profiles are studied. The velocity profiles have similar distributions under different interface conditions in the traditional wall configuration. The T/NT interface perspective provides an observation position to further investigate similar characteristics in the outer region. The results normalized by the boundary layer thickness show no differences under different interface conditions in the logarithmic region and below. Normalized by the local interface height, it is also found that the region close to the interface is not subject to interface conditions. The self-similarity relation $y' = f_{Y_i}(y)$ is given based on the exponential configuration, which emphasizes that the self-similarity relates to the wall-normal coordinates and the local interface height. This self-similarity relationship specifies the statistical association of the outer region features normalized according to the interface. The relationship is applicable in the low to moderate Reynolds number range ($\mathrm{Re}_\tau = 389$–1000). In this paper, we pay attention to the self-similarity in the region which is above the logarithmic region and does not include the region affected by the T/NT interface. The definition of the region relying on the interface is according to the inflection point of the raw velocity profile. The mean scale of the region dominated by the T/NT interface is 0.09δ.

The self-similar spatial distribution trend of the outer-layer structures is investigated. The results show similar spatial correlation contours at the corresponding wall-normal reference heights. The spatial two-point correlation emphasizes the spatial coherence of the turbulent fluctuations and reflects the spatial features of turbulent structures. The structural scale in the outer layer is measured with the criteria that the correlation coefficient is > 0.5. From the y' and y/Y_i frameworks, the structural scales at the corresponding reference heights exhibit good consistency for different interface height conditions. As the structures away from the wall, the wall-normal scale increases. Then the scale reaches its maximum. It decreases as it approaches the T/NT interface. This pattern of structural scale distribution is consistent with the knowledge gained so far on the wall frame vs the interface frame. The wall-normal scale variation of the outer-layer structure is fitted using the quadratic function. In the current Reynolds number range, the coefficient a is 0.70 ± 0.02 and b is 0.07 ± 0.01.

The conditional statistics of the TKE show a monotonically decreasing trend as the interface height increases. For the low-interface conditions, the TKE is higher than that for the high-interface conditions in the outer region. The static pressure in the turbulent region for the low-interface condition is lower than that in the non-turbulent region [22]. This leads to the interface height being lower than its mean value and the structure-based superposition effects of TKE. The energy superposition effect is specified with the reference to the spatial characteristics of the outer region structure. The effect is introduced in the region that is above the logarithmic region and far away enough from the interface. According to the energy superposition effect, the TKE is reconsidered. First, low interfaces imply stronger superposition effects, while high interfaces lead to the reduction of the energy superposition. Second, the effect is more obvious as it moves away from the wall and is diminished as it approaches the T/NT interface. The results reveal that the reconsidered TKE of the structure is self-similar at the corresponding reference height. The consistent distribution of the reconsidered TKE is observed for results based on both the self-similarity framework as well as the local interface height framework. It should be emphasized that the self-similarity framework better reveals the self-similar behavior of the TKE. The structure-based energy self-similarity augments the structural connotations of interface-based self-similarity properties of the outer-layer intermittent region.
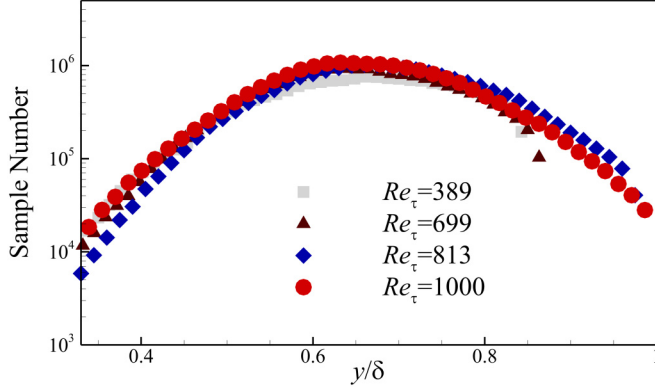
FIG. 13. The sample number for different interface locations.

APPENDIX: CONVERGENCE

The interface-based conditional statistics are accurate to spatial resolution of PIV. Therefore, it is necessary to consider the convergence of the database.

The total number of samples at all interface heights for the four cases is given in Fig. 13. The smallest number of samples is the lowest interface position of Case 3 (5859 samples), while all the sample numbers of other interface positions are $\sim 10^4$ or more. The maximum sample number is $> 10^6$. In the range $\{[E(Y_i) - 2\sigma(Y_i)]/\delta, [E(Y_i) + 2\sigma(Y_i)]/\delta\}$, the sample numbers are all $> 10^5$.
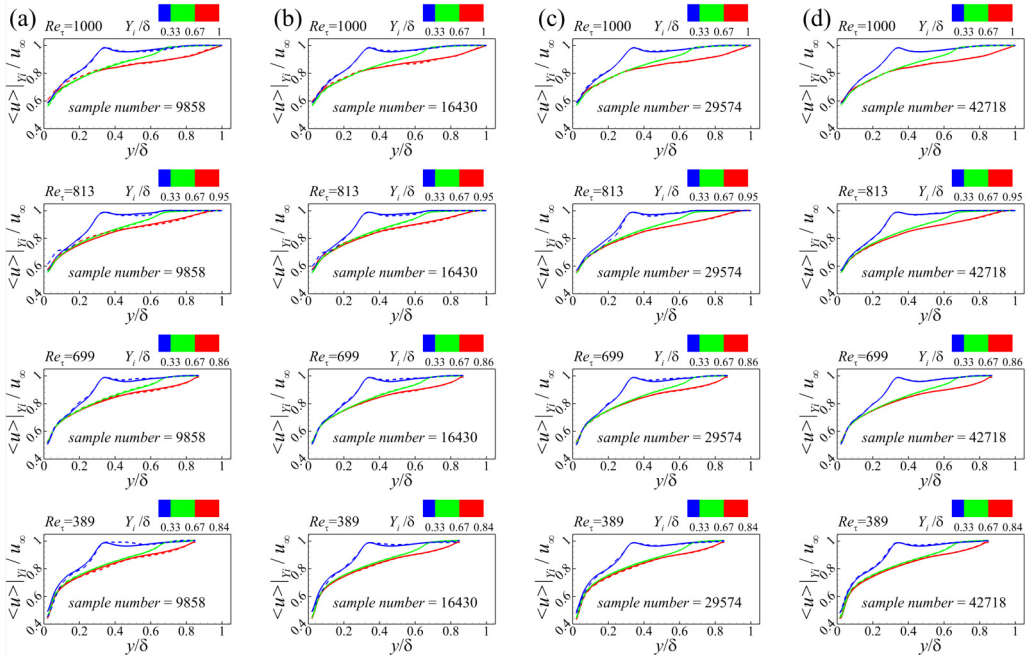

FIG. 14. Verification of convergence of conditional mean raw velocity. Blue line: The lowest interface location. Red line: The highest interface location. Green line: The mean interface location. The frame number of conditional statistics: 9858, 16 430, 29 574, and 42 718 frames, respectively. The dashed lines are the partial sample results, and the solid lines are the total sample results.
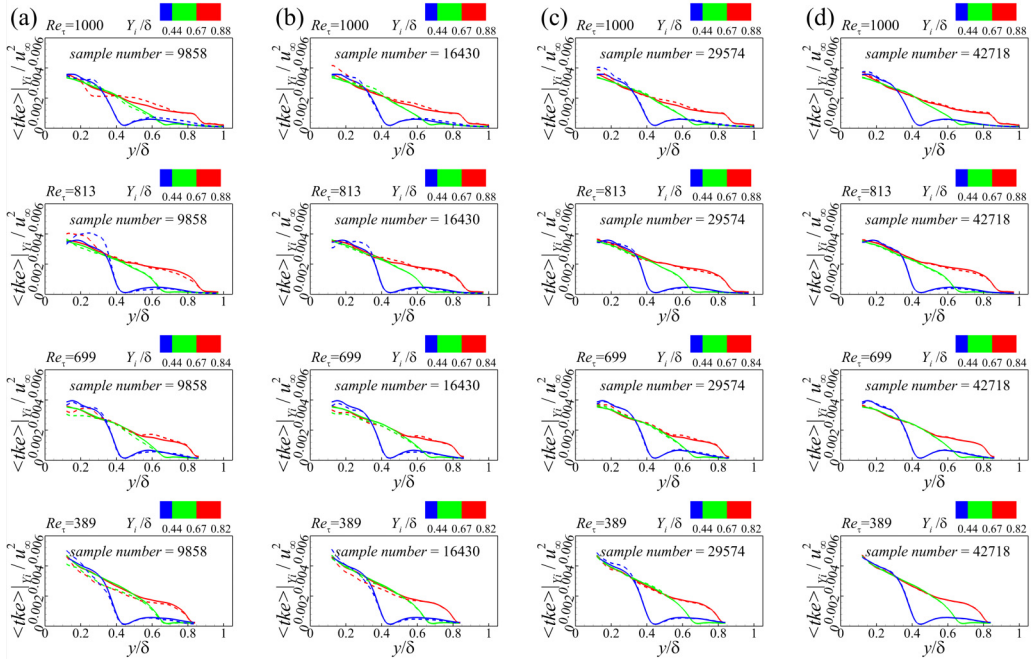
FIG. 15. Verification of convergence of conditional mean turbulent kinetic energy. Blue line: The lowest interface location. Red line: The highest interface location. Green line: The mean interface location. The frame number of conditional statistics: 9858, 16 430, 29 574, and 42 718 frames, respectively. The dashed lines are the partial sample results, and the solid lines are the total sample results.

Figures 14 and 15 illustrate the convergence of the conditional mean raw streamwise velocity and TKE for different interface locations. Figures 14 and 15 show the four cases in the vertical column. The number of samples participating in the statistics gradually increases in the horizontal row direction. Figure 14 shows the results for all interface conditions captured in the field of view. Figure 15 shows the results only in the range of $\{[E(Y_i) - 2\sigma(Y_i)]/\delta, [E(Y_i) + 2\sigma(Y_i)]/\delta\}$. The lowest (blue line) and highest (red line) interface locations, as well as the mean interface location (green line), are selected for reference. The lowest and highest interface locations are the most difficult to converge because of the Gaussian distribution of the interface. Convergence validation is performed by increasing the number of statistical samples. The control group is the whole sample (49 290 frames). The dashed lines are the partial sample results, and the solid lines are the total sample results. When the number of statistical frames reaches 42 718 frames, the results are consistent in the control group for the four cases. This means that the convergence of the conditional statistics can be guaranteed.

[1] S. Corrsin and A. L. Kistler, Free-stream boundaries of turbulent flows, NASA Technical Report 19930092246 (1955), https://ntrs.nasa.gov/citations/19930092246.

[2] H. Fiedler and M. R. Head, Intermittency measurements in the turbulent boundary layer, J. Fluid Mech. **25**, 719 (1966).

[3] R. J. Adrian, C. D. Meinhart, and C. D. Tomkins, Vortex organization in the outer region of the turbulent boundary layer, J. Fluid Mech. **422**, 1 (2000).

[4] I. Marusic, R. Mathis, and N. Hutchins, High Reynolds number effects in wall turbulence, Int. J. Heat Fluid Flow **31**, 418 (2010).

[5] P. Moin and K. Mahesh, Direct numerical simulation: A tool in turbulence research, Annu. Rev. Fluid Mech. **30**, 539 (1998).

[6] R. D. Moser, J. Kim, and N. N. Mansour, Direct numerical simulation of turbulent channel flow up to $Re_\tau = 590$, Phys. Fluids **11**, 943 (1999).

[7] J. Jiménez, S. Hoyas, M. P. Simens, and Y. Mizuno, Turbulent boundary layers and channels at moderate Reynolds numbers, J. Fluid Mech. **657**, 335 (2010).

[8] W. Schoppa and F. Hussain, Coherent structure generation in near-wall turbulence, J. Fluid Mech. **453**, 57 (2002).

[9] P. Schlatter, Q. Li, R. Örlü, F. Hussain, and D. S. Henningson, On the near-wall vortical structures at moderate Reynolds numbers, Eur. J. Mech. B. Fluids **48**, 75 (2014).

[10] C. E. Willert, C. Cuvier, J. M. Foucaut, J. Klinner, M. Stanislas, J. P. Laval, S. Srinath, J. Soria, O. Amili, C. Atkinson *et al.*, Experimental evidence of near-wall reverse flow events in a zero pressure gradient turbulent boundary layer, Exp. Therm. Fluid Sci. **91**, 320 (2018).

[11] R. J. Adrian and I. Marusic, Coherent structures in flow over hydraulic engineering surfaces, J. Hydraul. Res. **50**, 451 (2012).

[12] K. T. Christensen and R. J. Adrian, Statistical evidence of hairpin vortex packets in wall turbulence, J. Fluid Mech. **431**, 433 (2001).

[13] C. M. de Silva, N. Hutchins, and I. Marusic, Uniform momentum zones in turbulent boundary layers, J. Fluid Mech. **786**, 309 (2015).

[14] Z. Q. Tang, Z. Y. Fan, L. T. Chen, and N. Jiang, Outer-layer structure arrangements based on the large-scale zero-crossings at moderate Reynolds number, Phys. Fluids **33**, 085121 (2021).

[15] L. Wang, C. Pan, J. Wang, and Q. Gao, Statistical signatures of component wall-attached eddies in proper orthogonal decomposition modes of a turbulent boundary layer, J. Fluid Mech. **944**, A26 (2022).

[16] D. Coles, The law of the wake in the turbulent boundary layer, J. Fluid Mech. **1**, 191 (1956).

[17] L. S. G. Kovasznay, V. Kibens, and R. F. Blackwelder, Large-scale motion in the intermittent region of a turbulent boundary layer, J. Fluid Mech. **41**, 283 (1970).

[18] C. B. da Silva, J. C. R. Hunt, I. Eames, and J. Westerweel, Interfacial layers between regions of different turbulence intensity, Annu. Rev. Fluid Mech. **46**, 567 (2014).

[19] A. A. Townsend, The mechanism of entrainment in free turbulent flows, J. Fluid Mech. **26**, 689 (1966).

[20] D. Wu, J. Wang, G. Cui, and C. Pan, Effects of surface shapes on properties of turbulent/non-turbulent interface in turbulent boundary layers, Sci. China: Technol. Sci. **63**, 214 (2019).

[21] K. Chauhan, J. Philip, C. M. de Silva, N. Hutchins, and I. Marusic, The turbulent/non-turbulent interface and entrainment in a boundary layer, J. Fluid Mech. **742**, 119 (2014).

[22] N. Reuther and C. J. Kähler, Effect of the intermittency dynamics on single and multipoint statistics of turbulent boundary layers, J. Fluid Mech. **897**, A11 (2020).

[23] L. Chen, Z. Fan, Z. Tang, X. Wang, D. Shi, and N. Jiang, Outer-layer coherent structures from the turbulent/non-turbulent interface perspective at moderate Reynolds number, Exp. Therm. Fluid Sci. **140**, 110760 (2023).

[24] N. Hutchins and I. Marusic, Evidence of very long meandering features in the logarithmic region of turbulent boundary layers, J. Fluid Mech. **579**, 1 (2007).

[25] J. Lee, J. H. Lee, J.-I. Choi, and H. J. Sung, Spatial organization of large- and very-large-scale motions in a turbulent channel flow, J. Fluid Mech. **749**, 818 (2014).

[26] Z. X. Dong, C. Pan, J. J. Wang, and X. X. Yuan, Reduced-order representation of superstructures in a turbulent boundary layer, Phys. Fluids **35**, 055146 (2023).

[27] J. Lee, H. J. Sung, and T. A. Zaki, Signature of large-scale motions on turbulent/non-turbulent interface in boundary layers, J. Fluid Mech. **819**, 165 (2017).

[28] R. J. Adrian, Hairpin vortex organization in wall turbulence, Phys. Fluids **19**, 041301 (2007).

[29] C. M. de Silva, D. Chandran, R. Baidya, N. Hutchins, and I. Marusic, Periodicity of large-scale coherence in turbulent boundary layers, Int. J. Heat Fluid Flow **83**, 108575 (2020).

[30] Y. Fukunishi and H. Sato, Formation of intermittent region by coherent motions in the turbulent boundary layer: Coherent motions and intermittent region, Fluid Dyn. Res. **2**, 113 (1987).

[31] C. B. da Silva and R. J. dos Reis, The role of coherent vortices near the turbulent/non-turbulent interface in a planar jet, Philos. Trans. R. Soc. A **369**, 738 (2011).

[32] C. M. de Silva, J. Philip, K. Chauhan, C. Meneveau, and I. Marusic, Multiscale geometry and scaling of the turbulent-nonturbulent interface in high Reynolds number boundary layers, Phys. Rev. Lett. **111**, 044501 (2013).

[33] K. Chauhan, J. Philip, and I. Marusic, Scaling of the turbulent/non-turbulent interface in boundary layers, J. Fluid Mech. **751**, 298 (2014).

[34] G. Borrell and J. Jiménez, Properties of the turbulent/non-turbulent interface in boundary layers, J. Fluid Mech. **801**, 554 (2016).

[35] K. Kevin, J. P. Monty, H. L. Bai, G. Pathikonda, B. Nugroho, J. M. Barros, K. T. Christensen, and N. Hutchins, Cross-stream stereoscopic particle image velocimetry of a modified turbulent boundary layer over directional surface pattern, J. Fluid Mech. **813**, 412 (2017).

[36] T. S. Silva, M. Zecchetto, and C. B. da Silva, The scaling of the turbulent/non-turbulent interface at high Reynolds numbers, J. Fluid Mech. **843**, 156 (2018).

[37] D. J. C. Dennis and T. B. Nickels, Experimental measurement of large-scale three-dimensional structures in a turbulent boundary layer. Part 1. Vortex packets, J. Fluid Mech. **673**, 180 (2011).

[38] Y. S. Kwon, N. Hutchins, and J. P. Monty, On the use of the Reynolds decomposition in the intermittent region of turbulent boundary layers, J. Fluid Mech. **794**, 5 (2016).

[39] Z. Q. Tang, L. T. Chen, Z. Y. Fan, X. Y. Ma, and N. Jiang, Cross-term events of scale-decomposed skewness factor in turbulent boundary layer at moderate Reynolds number, Phys. Fluids **33**, 055124 (2021).

[40] Z. Fan, Z. Tang, X. Ma, and N. Jiang, Convection of multi-scale motions in turbulent boundary layer by temporal resolution particle image velocimetry, J. Turbul. **23**, 305 (2022).

[41] P. Schlatter and R. Örlü, Assessment of direct numerical simulation data of turbulent boundary layers, J. Fluid Mech. **659**, 116 (2010).

[42] D. K. Bisset, J. C. R. Hunt, and M. M. Rogers, The turbulent/non-turbulent interface bounding a far wake, J. Fluid Mech. **451**, 383 (2002).

[43] J. Westerweel, C. Fukushima, J. M. Pedersen, and J. C. R. Hunt, Momentum and scalar transport at the turbulent/non-turbulent interface of a jet, J. Fluid Mech. **631**, 199 (2009).

[44] T. Watanabe, Y. Sakai, K. Nagata, Y. Ito, and T. Hayase, Vortex stretching and compression near the turbulent/non-turbulent interface in a planar jet, J. Fluid Mech. **758**, 754 (2014).

[45] T. Watanabe, X. Zhang, and K. Nagata, Turbulent/non-turbulent interfaces detected in DNS of incompressible turbulent boundary layers, Phys. Fluids **30**, 035102 (2018).

[46] M. M. Neamtu-Halic, D. Krug, J.-P. Mollicone, M. van Reeuwijk, G. Haller, and M. Holzner, Connecting the time evolution of the turbulence interface to coherent structures, J. Fluid Mech. **898**, A3 (2020).

[47] M. Boetti, M. van Reeuwijk, and A. Liberzon, Potential-enstrophy lengthscale for the turbulent/nonturbulent interface in stratified flow, Phys. Rev. Fluids **6**, 114803 (2021).

[48] M. Gauding, M. Bode, Y. Brahami, É. Varea, and L. Danaila, Self-similarity of turbulent jet flows with internal and external intermittency, J. Fluid Mech. **919**, A41 (2021).

[49] R. K. Anand, B. J. Boersma, and A. Agrawal, Detection of turbulent/non-turbulent interface for an axisymmetric turbulent jet: Evaluation of known criteria and proposal of a new criterion, Exp. Fluids **47**, 995 (2009).

[50] C. M. de Silva, J. Philip, N. Hutchins, and I. Marusic, Interfaces of uniform momentum zones in turbulent boundary layers, J. Fluid Mech. **820**, 451 (2017).

[51] N. Reuther and C. J. Kahler, Evaluation of large-scale turbulent/non-turbulent interface detection methods for wall-bounded flows, Exp. Fluids **59**, 121 (2018).

[52] R. R. Prasad and K. R. Sreenivasan, Scalar interfaces in digital images of turbulent flows, Exp. Fluids **7**, 259 (1989).

[53] M. Gampert, J. Boschung, F. Hennig, M. Gauding, and N. Peters, The vorticity versus the scalar criterion for the detection of the turbulent/non-turbulent interface, J. Fluid Mech. **750**, 578 (2014).

[54] J. Philip, C. Meneveau, C. M. de Silva, and I. Marusic, Multiscale analysis of fluxes at the turbulent/non-turbulent interface in high Reynolds number boundary layers, Phys. Fluids **26**, 015105 (2014).

[55] D. Wu, J. Wang, and C. Pan, Bubbles and drops in the vicinity of turbulent/non-turbulent interface in turbulent boundary layers, Exp. Fluids **61**, 240 (2020).

[56] Z. Wu, J. Lee, C. Meneveau, and T. Zaki, Application of a self-organizing map to identify the turbulent-boundary-layer interface in a transitional flow, Phys. Rev. Fluids **4**, 023902 (2019).

[57] Y. Long, D. Wu, and J. Wang, A novel and robust method for the turbulent/non-turbulent interface detection, Exp. Fluids **62**, 138 (2021).

[58] K. Younes, B. Gibeau, S. Ghaemi, and J. P. Hickey, A fuzzy cluster method for turbulent/non-turbulent interface detection, Exp. Fluids **62**, 73 (2021).

[59] K. S. Kankanwadi and O. R. H. Buxton, Influence of freestream turbulence on the near-field growth of a turbulent cylinder wake: Turbulent entrainment and wake meandering, Phys. Rev. Fluids **8**, 034603 (2023).

[60] K. A. Chauhan, P. A. Monkewitz, and H. M. Nagib, Criteria for assessing experiments in zero pressure gradient boundary layers, Fluid Dyn. Res. **41**, 021404 (2009).

[61] N. V. Semin, V. V. Golub, G. E. Elsinga, and J. Westerweel, Laminar superlayer in a turbulent boundary layer, Tech. Phys. Lett. **37**, 1154 (2011).

[62] J. Eisma, J. Westerweel, G. Ooms, and G. E. Elsinga, Interfaces and internal layers in a turbulent boundary layer, Phys. Fluids **27**, 055103 (2015).

[63] O. Reynolds, IV. On the dynamical theory of incompressible viscous fluids and the determination of the criterion, Philos. Trans. R. Soc. Lond. A **186**, 123 (1895).

[64] S. Corrsin, Investigation of flow in an axially symmetrical heated jet of air, NASA Technical Report 19930090930 (1943), https://ntrs.nasa.gov/citations/19930090930.

[65] T. B. Hedleyt and J. F. Keffer, Some turbulent/non-turbulent properties of the outer intermittent region of a boundary layer, J. Fluid Mech. **64**, 645 (1972).

[66] A. K. M. F. Hussain and W. C. Reynolds, The mechanics of an organized wave in turbulent shear flow, J. Fluid Mech. **41**, 241 (1970).

[67] I. Marusic and J. P. Monty, Attached eddy model of wall turbulence, Annu. Rev. Fluid Mech. **51**, 49 (2019).

[68] A. E. Perry and M. S. Chong, On the mechanism of wall turbulence, J. Fluid Mech. **119**, 173 (1982).